
DIFFERENTIABLE ZOOMING FOR MULTIPLE INSTANCE LEARNING ON WHOLE-SLIDE IMAGES

A PREPRINT

**Kevin Thandiackal^{1,2*}, Boqi Chen^{1,2*}, Pushpak Pati¹, Guillaume Jaume³
Drew F. K. Williamson^{4,5}, Maria Gabrani¹, Orcun Goksel^{2,6}**

¹IBM Research Europe, Zurich, Switzerland

²Computer-assisted Applications in Medicine, ETH Zurich, Zurich, Switzerland

³Signal Processing Laboratory 5, EPFL, Lausanne, Switzerland

⁴Brigham and Women's Hospital, Boston, United States

⁵Harvard Medical School, Boston, United States

⁶Department of Information Technology, Uppsala University, Uppsala, Sweden

ABSTRACT

Multiple Instance Learning (MIL) methods have become increasingly popular for classifying gigapixel sized Whole-Slide Images (WSIs) in digital pathology. Most MIL methods operate at a *single* WSI magnification, by processing *all* the tissue patches. Such a formulation induces high computational requirements, and constrains the contextualization of the WSI-level representation to a single scale. A few MIL methods extend to multiple scales, but are computationally more demanding. In this paper, inspired by the pathological diagnostic process, we propose ZOOMBIL, a method that *learns* to perform multi-level zooming in an end-to-end manner. ZOOMBIL builds WSI representations by aggregating tissue-context information from multiple magnifications. The proposed method outperforms the state-of-the-art MIL methods in WSI classification on two large datasets, while significantly reducing the computational demands with regard to Floating-Point Operations (FLOPs) and processing time by up to 40 \times .

Keywords Whole-Slide Image Classification · Multiple Instance Learning · Multi-scale Zooming · Efficient Computational Pathology

1 Introduction

Histopathological diagnosis requires a pathologist to examine tissue to characterize the phenotypic, morphologic, and topologic distribution of the tissue constituents. With advancements in slide-scanning technologies, tissue specimens can now be digitized into Whole-Slide Images (WSIs) with impressive resolution, enabling the pathological assessment to be conducted on a computer screen rather than under a microscope. As does a glass slide, a WSI contains rich tissue information, and can be up to 100 000 \times 100 000 pixels in size at 40 \times magnification (0.25 μ m/pixel). Due to image size and complexity as well as the multi-scale nature of biological systems, a pathologist generally examines the slide in a hierarchical manner, beginning with the detection of informative regions at a *low* magnification, followed by a detailed evaluation of selected areas at a *high* magnification, as exemplified in Figure 1(a). However, depending on the tissue sample, such manual examination of a gigapixel-sized WSI can be cumbersome, time-consuming, and prone to inter- and intra-observer variability [Gomes et al., 2014; Elmore et al., 2015].

To alleviate the aforementioned challenges, Deep Learning (DL) based diagnosis tools are being developed in digital pathology. However, these tools encounter additional challenges pertaining to the large size of the WSIs, and the difficulty of acquiring fine-grained, pixel-level annotations. To address these, dedicated DL methods have been proposed, in particular based on Multiple Instance Learning (MIL). In MIL, a WSI is first decomposed into a bag of patches, which

*The authors contributed equally to this work.

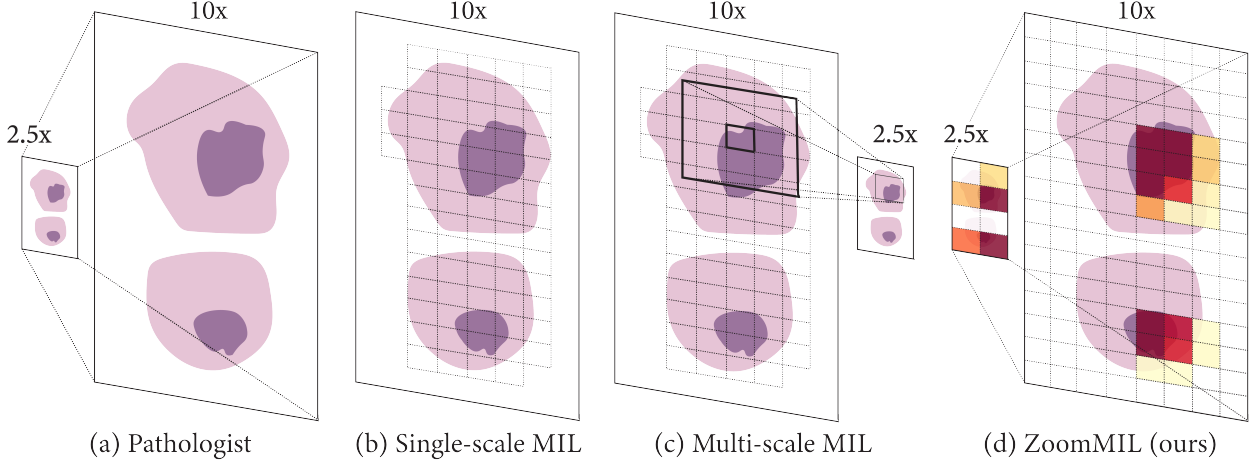


Figure 1: Comparison of different methods for the diagnosis of WSIs

are individually encoded by a backbone Convolutional Neural Network (CNN). Then, a pooling operation combines the resulting patch embeddings to produce a slide-level representation that is finally mapped to the bag/image label. Although these approaches have achieved remarkable performance on a variety of pathology tasks, such as tumor classification [Campanella et al., 2019; Lu et al., 2021a; Tellez et al., 2019; Shaban et al., 2020], tumor segmentation [Jia et al., 2017; Liang et al., 2018], and survival prediction [Yao et al., 2020], they pose the following drawbacks.

First, the performance of an MIL method relies on a carefully tuned context-resolution trade-off [Pati et al., 2021; Bejnordi et al., 2017a; Sirinukunwattana et al., 2018], *i.e.*, an optimal resolution of operation while including adequate context in a patch. As the dimensions of diagnostically relevant tissue constituents vary significantly in histopathology, patches of different sizes at different magnifications render different context information about the tissue microenvironment. Thus, identifying an optimal resolution and patch size involves several tailored and tedious steps. Typical MIL methods work with patches at a *single* magnification, as shown in Figure 1(b), and disregard the spatial distribution of the patches, leading to the above problem. Though some MIL methods address this trade-off via visual self-attention [Myronenko et al., 2021; Shao et al., 2021], they are constrained by the expensive computation of attention scores on a large number of patches in a WSI. Differently, [Lerousseau et al., 2021] addresses the issue via random patch sampling and sparse-convolutions, which consequently prevents deterministic inference. In the literature, other methods [Sirinukunwattana et al., 2018; Hashimoto et al., 2020; Ho et al., 2021] are proposed based on the concept of concentric-patches across multiple magnifications, as shown in Figure 1(c), to acquire richer context per patch. However, these methods are computationally more expensive as they require to encode all the patches at a high magnification and all the corresponding patches across other lower magnifications.

Second, MIL approaches process *all* the tissue patches at a high magnification. Thus, a large number of uninformative patches are processed, increasing the computational cost, inference time, and memory requirements. For instance, inferring on a WSI of $50\,000 \times 50\,000$ pixels by CLAM [Lu et al., 2021a], an MIL method, requires ≈ 150 Tera Floating-Point Operations (FLOPs), which is $37\,500 \times$ the processing of an ImageNet [Deng et al., 2009] sample by ResNet34 [He et al., 2016]. Further, the high memory footprint of these methods inhibits their scalability to large histopathology images, *e.g.*, prostatectomy slides which can be of $300\,000 \times 400\,000$ pixels at $40\times$ magnification. Such requirements of intensive computational resources, can in turn hinder the clinical deployment of these approaches. Their adoption becomes even prohibitive when the computational resources are scarce owing to a limited access to GPUs or cloud services. In view of the above challenges with the existing MIL methods, a multi-scale context-aware MIL method with a high computational efficiency is desired.

In this paper we propose ZOOMMIL, a novel method inspired by the hierarchical diagnostic process of pathologists, to address the above drawbacks with MIL. We first identify Regions-of-Interest (ROIs) at a low magnification, and then zoom in on them at a high magnification for fine-grained analysis, as shown in Figure 1(d). The ROI selection is performed through a gated-attention and a differentiable top-K (DIFF-TOPK) module, which allows to learn where to zoom in, in an end-to-end manner, while moderating the computational requirements at high magnifications. This process can be repeated across an arbitrary number of magnifications, *e.g.*, $5\times \rightarrow 10\times \rightarrow 20\times$, as per the application at hand. Finally, we aggregate the information acquired across multiple scales to obtain a context-aware WSI representation to perform downstream pathology tasks, as presented in Figure 2. In summary, our contributions are:

1. A novel multi-scale context-aware MIL method that learns to perform multi-level zooming in an end-to-end manner for WSI classification.
2. A computationally much more efficient method compared to the state of the art in MIL, *e.g.*, $40\times$ faster inference on a WSI of size $26\,009\times 18\,234$ pixels at $10\times$ magnification, while achieving better (2/3 datasets) or comparable (1/3 datasets) WSI classification performance.
3. Comprehensive benchmarking of the method with regard to WSI classification performance and computational requirements (on GPU and CPU) on multiple datasets across multiple organs and pathology tasks, *i.e.*, tumor subtyping, grading, and metastasis detection.

2 Related Work

2.1 Multiple Instance Learning in Histopathology

MIL in histopathology was introduced in [Isle et al., 2018] to classify breast and colon RoIs. The experiments established the superiority of *attention*-based pooling over vanilla *max* and *mean* pooling operations. Concurrently, [Campanella et al., 2019] scaled MIL to WSI-level for grading prostate needle biopsies. This work proposed the use of end-to-end training with Recurrent Neural Network (RNN)-based pooling. Later, several works consolidated attention-based MIL by applying it across several organs and pathology tasks, *e.g.*, [Yao et al., 2020; Lu et al., 2021a,b]. Recently, transformer-based MIL methods [Myronenko et al., 2021; Shao et al., 2021] were proposed to take into account the inter-patch dependencies, with the downside of having to compute a quadratic number of interactions, which introduces memory constraints. Additionally, all the aforementioned MIL methods are limited to operate on *all* the patches in a WSI at a single magnification. In view of the benefits of multi-scale information in histopathology image analysis [Bejnordi et al., 2015; Gao et al., 2016; Tokunaga et al., 2019; Li et al., 2021a; Ho et al., 2021; Pati et al., 2021], a few recent methods [Hashimoto et al., 2020; Li et al., 2021b] were proposed to extend the MIL methods to combine information across multiple magnifications. However, similar to the single-scale methods, these multi-scale versions also require to process *all* the patches in a WSI, which is computationally more expensive. In contrast, our proposed ZOOMBIL *learns* to identify informative regions at low magnification, and subsequently zooms into these regions at high magnification for efficient and comprehensive analysis. Differently, several other approaches aim to learn the inter-instance relations in histopathology via Graph Neural Networks (GNNs) [Aygüneş et al., 2020; Pati et al., 2021; Zhao et al., 2020; Raju et al., 2020; Li et al., 2018; Adnan et al., 2020; Anklin et al., 2021] or CNNs [Tellez et al., 2019; Shaban et al., 2020; Lerousseau et al., 2021].

2.2 Instance Selection Strategies in Histopathology

Most MIL methods encode all the patches in a WSI irrespective of their functional types. This definition compels MIL to be computationally expensive for large WSIs in histopathology. To reduce the computational memory requirement, [Lerousseau et al., 2021] proposed to randomly sample a subset of instances, with the consequence of potentially missing vital information, especially when the informative set is small, *e.g.*, metastasis detection. Differently, a few reinforcement learning-based methods [Dong et al., 2018; Qaiser and Rajpoot, 2019] were proposed to this end. [Qaiser and Rajpoot, 2019] proposed to sequentially identify some of the diagnostically relevant RoIs in a WSI by following a parameterized policy. However, the method leverages a very coarse context information for the ROI identification, and is limited to utilize only single-scale information for the diagnosis. Additionally, the reinforcement learning method in [Dong et al., 2018] and the recurrent visual attention-based model in [BenTaieb and Hamarneh, 2018] aim to select patches which mimics pathological diagnosis. However, these methods require pixel-level annotations for learning discriminative regions, which is expensive to acquire on large WSIs. In contrast to the above methods, ZOOMBIL requires only WSI-level supervision. Our method is flexible to attend to several magnifications, while efficiently classifying WSIs with high performance.

The attention-score-based iterative sampling strategy proposed in [Kong and Henao, 2021; Katharopoulos and Fleuret, 2019] closely relates to our work. For the final classification, the selected patch embeddings are simply concatenated, analogous to average pooling. Instead, ZOOMBIL incorporates a dual gated-attention module between two consecutive magnifications to simultaneously learn to select the relevant instances to be zoomed into, and learn an improved WSI-level representation for the lower magnification.

The patch selection module employed in our work is inspired by the perturbed optimizer-based [Berthet et al., 2020] differentiable Top-K algorithm proposed in [Cordonnier et al., 2021]. ZOOMBIL advances upon [Cordonnier et al., 2021] by extending to several magnifications, *i.e.*, multi-level zooming, and scaling the applications to giga-pixel sized WSIs.

3 MIL with Differentiable Zooming

In this section, we present our differentiable zooming approach, that first identifies informative patches at a low magnification and afterwards zooms into them for fine-grained analysis. In Sec. 3.1, we introduce the gated-attention mechanism that determines the informative patches at a magnification. In Sec. 3.2, we describe how to enable the attention-based patch selection to be differentiable while employing multiple magnifications. Finally, we present in Sec. 3.3 our overall architecture, in particular our proposed Dual Gated Attention and multi-scale information aggregation.

3.1 Attention-based MIL

In MIL, an input X is considered as a bag of multiple instances, denoted as $X = \{\mathbf{x}_1, \dots, \mathbf{x}_N\}$. Given a classification task with C labels, there exists an *unknown* label $\mathbf{y}_i \in C$ for each instance and a *known* label $\mathbf{y} \in C$ for the bag. In our context, the input is a WSI and the instances denote the set of extracted patches. We follow the embedding-based MIL approaches [Isle et al., 2018; Lu et al., 2021a; Shao et al., 2021], where a patch-level feature extractor h maps each patch \mathbf{x}_i to a feature vector $\mathbf{h}_i = h(\mathbf{x}_i) \in \mathbb{R}^D$. Afterwards, a pooling operator $g(\cdot)$ aggregates the feature vectors $\mathbf{h}_{i=1:N}$ to produce a single WSI-level feature representation. Finally, a classifier $f(\cdot)$ uses the WSI representation to predict the WSI-level label $\hat{\mathbf{y}} \in C$. The end-to-end process can be summarized as:

$$\hat{\mathbf{y}} = f\left(g\left(\{h(\mathbf{x}_1), \dots, h(\mathbf{x}_N)\}\right)\right). \quad (1)$$

To aggregate the patch features, we employ an attention-pooling operation, specifically, the Gated Attention (GA) mechanism introduced in [Isle et al., 2018]. Let $\mathbf{H} = [\mathbf{h}_1, \dots, \mathbf{h}_N]^\top \in \mathbb{R}^{N \times D}$ be the patch-level feature matrix, then the WSI-level representation \mathbf{g} is computed as:

$$\mathbf{g} = \sum_{i=1}^N a_i \mathbf{h}_i, \quad a_i = \frac{\exp\{\mathbf{w}^\top (\tanh(\mathbf{V}\mathbf{h}_i) \odot \eta(\mathbf{U}\mathbf{h}_i))\}}{\sum_{j=1}^N \exp\{\mathbf{w}^\top (\tanh(\mathbf{V}\mathbf{h}_j) \odot \eta(\mathbf{U}\mathbf{h}_j))\}}, \quad (2)$$

where $\mathbf{w} \in \mathbb{R}^{L \times 1}$, $\mathbf{V} \in \mathbb{R}^{L \times D}$, $\mathbf{U} \in \mathbb{R}^{L \times D}$ are learnable parameters with hidden dimension L , \odot is element-wise multiplication, and $\eta(\cdot)$ is the sigmoid function. While previous attention-based MIL methods [Isle et al., 2018; Lu et al., 2021a] are designed to operate at only a *single* magnification, we propose an efficient and flexible MIL framework that can be extended to an arbitrary number of magnifications while being fully differentiable.

3.2 Attending to Multiple Magnifications

Let us assume the WSI is accessible at multiple magnifications, indexed by $m \in \{1, 2, \dots, M\}$, where M depicts the highest magnification. Consistent with the pyramidal format of WSIs, we assume the magnification at $m+1$ is twice the magnification at m . To efficiently extend MIL to multiple magnifications, we propose to hierarchically identify informative patches from low-to-high magnifications, and aggregate their features to get the WSI representation. To identify the informative patches at m , we first compute $\mathbf{a}_m \in \mathbb{R}^N$, that includes an attention score for each patch. Then, the top K patches with the highest attention scores are selected for further processing at a higher magnification. The corresponding selected patch feature matrix can be denoted by,

$$\tilde{\mathbf{H}}_m = \mathbf{T}_m^\top \mathbf{H}_m, \quad (3)$$

where $\mathbf{T}_m \in \{0, 1\}^{N \times K}$ is an indicator matrix, and $\mathbf{H}_m \in \mathbb{R}^{N \times D}$ is the patch feature matrix at m .

Instead of a handcrafted approach, we propose to drive the patch selection at m directly by the prediction output of $f(\cdot)$. This can be trivially achieved via a backpropagation path from the output of $f(\cdot)$ to the attention module at m , without introducing any additional loss or associated hyperparameters. However, this naive formulation is non-differentiable as it involves a Top-K operation. To address this problem, we build on the perturbed maximum method [Berthet et al., 2020] to make the Top-K selection differentiable, inspired by [Cordonnier et al., 2021], and apply it to the attention weights \mathbf{a}_m at magnification m . Specifically, \mathbf{a}_m is first perturbed by adding uniform Gaussian noise $\mathbf{Z} \in \mathbb{R}^N$. Then, a linear program is solved for each of these perturbed attention weights, and their results are averaged. Thus, the forward pass of the differentiable Top-K module can be written as:

$$\mathbf{T} = \mathbb{E}_{\mathbf{Z} \sim \mathcal{N}(0, \mathbf{I})} \left[\arg \max_{\hat{\mathbf{T}}} \langle \hat{\mathbf{T}}, (\mathbf{a}_m + \sigma \mathbf{Z}) \mathbf{1}^\top \rangle \right], \quad (4)$$

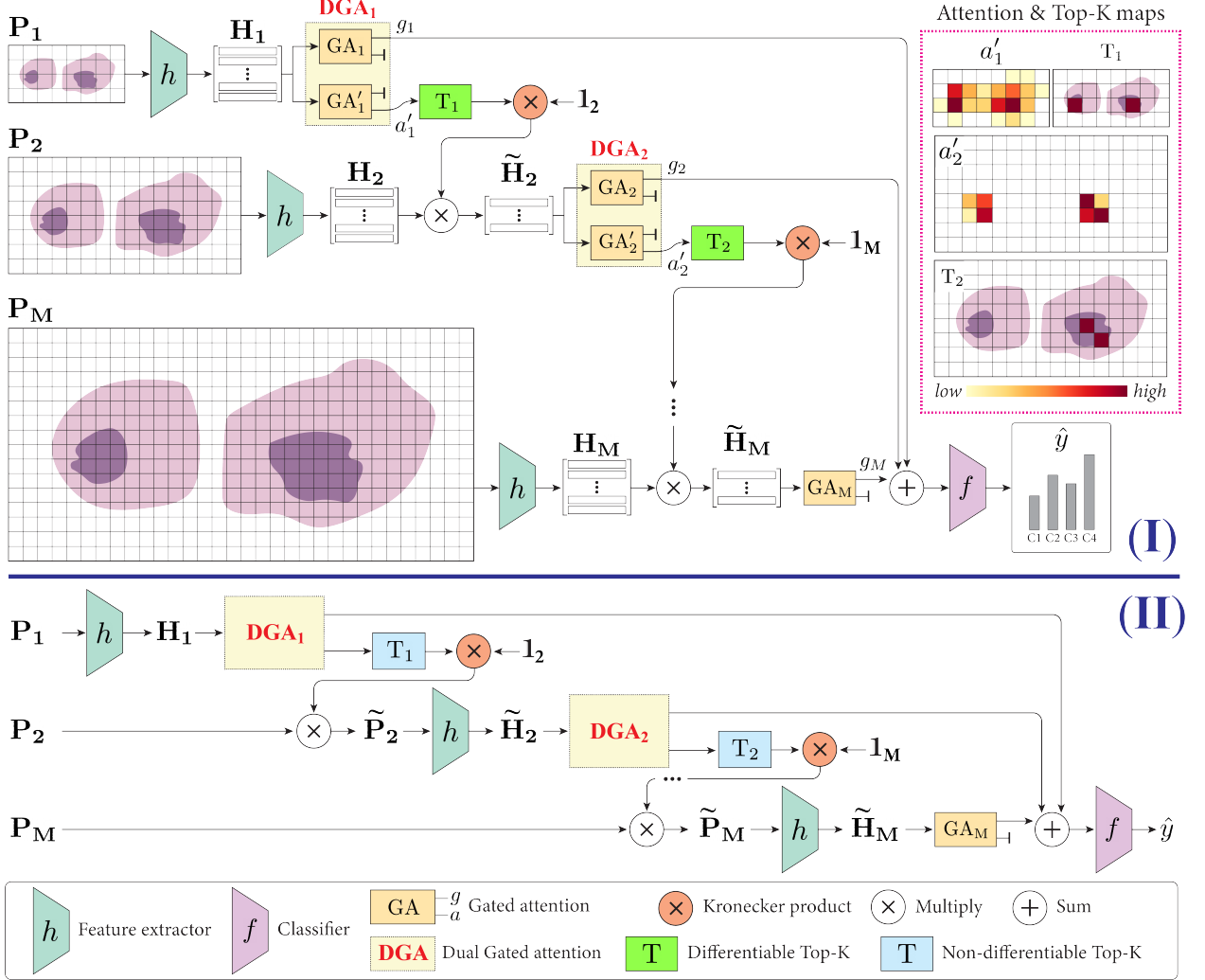


Figure 2: Overview of the proposed ZOOMMIL. (I) and (II) present the distinct training and inference modes, generically exemplified for M magnifications

where $\mathbf{1}^\top = [1 \cdots 1] \in \mathbb{R}^{1 \times K}$ and consequently $(\mathbf{a}_m + \sigma \mathbf{Z})\mathbf{1}^\top \in \mathbb{R}^{N \times K}$ denotes the perturbed attention weights repeated K times, and $\langle \cdot \rangle$ is a scalar product preceded by a vectorization of the matrices. The corresponding Jacobian is defined as:

$$J_{\mathbf{a}_m} \mathbf{T} = \mathbb{E}_{\mathbf{Z} \sim \mathcal{N}(0, \mathbf{I})} \left[\arg \max_{\tilde{\mathbf{T}}} \langle \tilde{\mathbf{T}}, (\mathbf{a}_m + \sigma \mathbf{Z})\mathbf{1}^\top \rangle \mathbf{Z}^\top / \sigma \right]. \quad (5)$$

More details on the derivation are provided in the supplemental material. The differentiable Top-K operator enables to *learn* the parameters of the attention module that weighs the patches at the specific magnification. Notably, we maintain a constant patch size across all magnifications, unlike [Cordonnier et al., 2021], which proportionately scales the patch sizes across magnifications. This proportionates the number of patches to the magnifications of operation. It also allows different fields-of-view of the tissue microenvironment across different magnifications, and enables to capture a variety of context information. This is a crucial requirement for analyzing histopathology slides as they contain diagnostically relevant constituents of various sizes. To achieve the objective of zooming, we propose to expand the indicator matrix \mathbf{T}_m in order to select from the patch features $\mathbf{H}_{m'} \in \mathbb{R}^{N \cdot 4^{(m'-1)} \times D}$, where $m' > m$. Specifically, we compute the Kronecker product between \mathbf{T}_m and the identity matrix $\mathbb{1}_{m'} = \text{diag}(1, \dots, 1) \in \mathbb{R}^{4^{(m'-1)} \times 4^{(m'-1)}}$ to yield the expanded indicator matrix $\mathbf{T}_{m'} \in \{0, 1\}^{N \cdot 4^{(m'-1)} \times K \cdot 4^{(m'-1)}}$. Analogously to Eq. (3), the patch selection at higher magnification m' using the attention weights from a lower magnification m can be performed by using,

$$\tilde{\mathbf{H}}_{m'} = (\mathbf{T}_m \otimes \mathbb{1}_{m'})^\top \mathbf{H}_{m'}, \quad (6)$$

where $\mathbf{H}_{m'}$ is the feature matrix at m' and $\tilde{\mathbf{H}}_{m'}$ is the selected feature matrix.

3.3 Dual Gated Attention and Multi-Scale Aggregation

An overview of our method is presented in Figure 2. The model has two distinct operational modes for training and inference, indicated as **(I)** and **(II)**.

Training mode: During training, the feature matrix \mathbf{H}_1 at $m=1$ passes through a Dual Gated Attention (DGA) block. DGA consists of two separate gated-attention modules GA_1 and GA'_1 . GA_1 is trained to obtain an optimal attention-pooled WSI-level representation \mathbf{g}_1 at low magnification. GA'_1 aims to provide meaningful attention weights \mathbf{a}'_1 to facilitate the patch selection for the next higher magnification. Alternatively, a single attention module could be employed to address both the tasks. However, this prevents the notion of optimal zooming, as the selected patches at the low magnification, to be zoomed-in, aim to optimize the classification performance of operating at the low magnification. Employing separate attention modules decouples the optimization tasks, and in turn, enables to obtain *complementary* information from both magnifications. Subsequently, the differentiable Top-K selection module, \mathbf{T}_1 , is employed to learn to select the most informative patches. The following selected higher magnification patch feature matrix $\tilde{\mathbf{H}}_2$ is obtained via Eq. (6).

The process of selecting patch features for every subsequent higher magnification is repeated until the highest magnification level M is reached. The selected patch features $\tilde{\mathbf{H}}_M$ at M go through a last gated-attention block GA_M to produce the high magnification feature representation \mathbf{g}_M . Finally, the attention-pooled feature representations from all magnifications, $\mathbf{g}_1, \mathbf{g}_2, \dots, \mathbf{g}_M$, are aggregated via sum-pooling to get a multi-scale, context-aware representation for the WSI. Inspired by residual learning [He et al., 2016], sum-pooling is employed as the features across different magnifications are closely related and the summation utilizes their complementarity. The final classifier $f(\cdot)$ maps the WSI representation to the WSI label $y \in C$, and produces the model prediction \hat{y} . The training phase can be regarded as extending Eq. (1) with sum-pooling over multiple magnifications:

$$\hat{y} = f\left(\mathbf{g}_1(\mathbf{H}_1) + \mathbf{g}_2(\tilde{\mathbf{H}}_2), \dots + \mathbf{g}_M(\tilde{\mathbf{H}}_M)\right). \quad (7)$$

Inference mode: We introduce the differentiable Top-K operator in our model during training to learn to identify informative patches. However, this operator includes random perturbations to the attention weights, and consequently makes the forward pass of the model non-deterministic. Therefore, we replace the differentiable Top-K with the conventional non-differentiable Top-K operator. Additionally, non-differentiable Top-K is faster as no perturbations have to be computed. As shown in Figure 2, another crucial difference to the training mode is that the patch selection directly operates on the WSI patches, $\mathbf{P}_{m'} \in \mathbb{R}^{N \cdot 4^{(m'-1)} \times p_h \times p_w \times p_c}$, instead of the pre-extracted patch features $\mathbf{H}_{m'}$. This avoids the extraction of features for uninformative patches during inference, unlike other MIL methods. It significantly reduces the computational requirements and speeds up model inference.

4 Experiments

4.1 Datasets

We benchmark our ZOONMIL on three H&E stained, public WSI datasets.

INSEC [Oliveira et al., 2021] contains 1133 colorectal biopsy and polypectomy slides from *non-neoplastic*, *low-grade*, and *high-grade* lesions, accounting for 26.5%, 48.7%, 24.8% of the data. The slides were acquired at the IMP Diagnostics laboratory, Portugal, and were digitized by a Leica GT450 scanner at 40 \times . We split the data into 70%/10%/20% stratified sets for training, validation, and testing.

BRIGHT [Brancati et al., 2021] consists of breast WSIs from *non-cancerous*, *precancerous*, and *cancerous* subtypes. The slides were acquired at the Fondazione G. Pascale, Italy, and scanned by Aperio AT2 scanner at 40 \times . We used the BRIGHT challenge splits² containing 423, 80, and 200 WSIs for train, validation, and testing.

CAMELYON16 [Bejnordi et al., 2017b] includes 270 WSIs, 160 normal and 110 with metastases, for training, and 129 slides for testing. The slides were scanned by 3DHISTECH and Hamamatsu scanners at 40 \times at the Radboud University Medical Center and the University Medical Center Utrecht, Netherlands. We split the 270 slides into 90%/10% stratified sets for training and validation.

The average number of (pixels, patches), within the tissue area, at 20 \times magnification for INSEC, BRIGHT, and CAMELYON16 datasets are (227.28 Mpx, 3468), (1.04 Gpx, 15872), and (648.28 Mpx, 9892), respectively.

²www.research.ibm.com/haifa/Workshops/BRIGHT

Table 1: Performance and efficiency measurement on INSEC dataset [Oliveira et al., 2021]. The best and the second best classification results are in **bold** and underline, respectively

Methods	Classification		Computation	
	Weighted-F1(%)	Accuracy(%)	TFLOPs	Time(s)
MAXMIL [Lerousseau et al., 2021] (20 \times)	82.2 \pm 0.9	82.2 \pm 1.2	0.96	0.06
MEANMIL [Lerousseau et al., 2021] (20 \times)	84.3 \pm 0.8	84.1 \pm 1.2	0.96	0.06
SPARSECONVMIL [Lerousseau et al., 2021] (20 \times)	89.6 \pm 1.3	89.6 \pm 0.9	0.96	0.06
ABMIL [Isle et al., 2018] (20 \times)	90.1 \pm 0.6	90.2 \pm 0.5	13.63	4.85
CLAM-SB [Lu et al., 2021a] (20 \times)	<u>90.9\pm0.6</u>	<u>90.9\pm0.5</u>	13.63	4.85
TRANSMIL [Shao et al., 2021] (20 \times)	89.8 \pm 1.1	90.2 \pm 0.9	13.63	4.85
ZOONMIL-EFF (5 \times \rightarrow 10 \times)	90.3 \pm 1.3	90.3 \pm 1.3	1.06	0.38
ZOONMIL (5 \times \rightarrow 10 \times \rightarrow 20 \times)	92.0\pm0.6	92.1\pm0.7	1.40	0.50

4.2 Implementation details

Preprocessing: For each WSI, we detect the tissue area using a Gaussian tissue detector [Jaume et al., 2021], and divide the tissue into patches of size 256 \times 256 at all considered magnifications. We ensure that each high magnification patch is associated to the corresponding lower magnification patch. We encode the patches with a ResNet-50 [He et al., 2016] pre-trained on ImageNet [Deng et al., 2009] and apply adaptive average pooling after the third residual block to obtain 1024-dimensional embeddings.

ZOONMIL: The gated-attention module comprises three 2-layer Multi-Layer Perceptrons (MLPs), where the first two are followed by Hyperbolic Tangent and Sigmoid activations, respectively. The classifier is a 2-layer MLP with ReLU activation. We use a dropout probability of 0.25 in all fully-connected layers.

Implementation: All methods are implemented using PyTorch [Paszke et al., 2019] and experiments are run on a single NVIDIA A100 GPU. ZOONMIL uses $K = \{16, 12, 300\}$ on INSEC, BRIGHT, and CAMELYON16, respectively, and ZOONMIL-EFF uses $K = \{12, 8\}$ on INSEC and BRIGHT, respectively. We use the Adam optimizer [Kingma and Ba, 2015] with 0.0001 learning rate and plateau scheduler (patience=5 epochs, decay rate=0.8). The experiments are run for 100 epochs with a batch size of one. The models with the best weighted F1-score (for BRIGHT) and best loss (for INSEC & CAMELYON16) on the validation set are saved for testing.

4.3 Results and Discussion

Baselines: We compare ZOONMIL with state-of-the-art MIL methods. Specifically, we compare with ABMIL [Isle et al., 2018], which uses a gated-attention pooling, and its variant CLAM [Lu et al., 2021a], which further includes an instance-level clustering loss. We further compare with two spatially-aware methods, namely, TRANSMIL [Shao et al., 2021] which models instance-level dependencies by pooling based on transformer blocks, and SPARSECONVMIL [Lerousseau et al., 2021] which uses sparse convolutions for pooling. For completeness, we also include vanilla MIL methods using max-pooling (MAXMIL) [Lerousseau et al., 2021] and mean-pooling (MEANMIL) [Lerousseau et al., 2021]. Notably, we do not compare against multi-scale MIL methods, *e.g.*, [Hashimoto et al., 2020; Li et al., 2021b], as they encode all patches in a WSI across all considered magnifications. This is computationally very inefficient, thereby limiting their applicability in practice. Individual implementation details and hyper-parameters of these baselines are provided in the supplemental material. For a fair comparison, preprocessing including the extraction of patch embeddings is done consistently in the same manner, as described in Section 4.2.

4.3.1 WSI classification performance

We present the classification results, in terms of weighted F1-score and accuracy, on INSEC, BRIGHT, and CAMELYON16 in Table 1, 2, and 3. Mean \pm standard deviation of the metrics are computed over three runs with different weight initializations. The corresponding magnifications of operation are shown alongside each method for each dataset. We include two versions of ZOONMIL using either 2 or 3 magnifications on INSEC and BRIGHT, denoted as ZOONMIL-EFF (efficient) and ZOONMIL.

On INSEC, ZOONMIL outperforms CLAM-SB and TRANSMIL by 1.1% and 2.2% weighted F1-score, respectively. Our efficient version achieves performance comparable to CLAM-SB and TRANSMIL, and obtains 1.7% lower weighted F1 than ZOONMIL. For the individual classes, *i.e.*, non-neoplastic, low-grade, and high-grade, ZOONMIL achieves 94.3%, 93.6%, and 86.4% average F1-scores in the one-vs-rest setting, respectively.

Table 2: Performance and efficiency measurement on BRIGHT dataset [Brancati et al., 2021]. The best and the second best classification results are in **bold** and underline, respectively

Methods	Classification		Computation	
	Weighted-F1	Accuracy	TFLOPs	Time(s)
MAXMIL [Lerousseau et al., 2021] (10 \times)	46.8 \pm 3.7	51.3 \pm 1.7	0.96	0.06
MEANMIL [Lerousseau et al., 2021] (10 \times)	44.9 \pm 2.8	47.1 \pm 0.1	0.96	0.06
SPARSECONVMIL [Lerousseau et al., 2021] (10 \times)	53.2 \pm 3.6	55.3 \pm 3.7	0.96	0.06
ABMIL [Isle et al., 2018] (10 \times)	63.5 \pm 2.7	65.5 \pm 1.9	16.45	5.86
CLAM-SB [Lu et al., 2021a] (10 \times)	63.1 \pm 1.7	64.3 \pm 1.7	16.45	5.86
TRANSMIL [Shao et al., 2021] (10 \times)	65.5 \pm 2.8	66.0 \pm 2.7	16.46	5.86
ZOONMIL-EFF (1.25 \times \rightarrow 2.5 \times)	<u>66.0\pm1.9</u>	<u>66.5\pm1.5</u>	0.40	0.14
ZOONMIL (1.25 \times \rightarrow 2.5 \times \rightarrow 10 \times)	68.3\pm1.1	69.3\pm1.0	1.29	0.46

Table 3: Performance and efficiency measurement on CAMELYON16 dataset [Bejnordi et al., 2017b]. The best and the second best classification results are in **bold** and underline, respectively

Methods	Classification		Computation	
	Weighted-F1(%)	Accuracy(%)	TFLOPs	Time(s)
MAXMIL[Lerousseau et al., 2021] (20 \times)	64.0 \pm 3.0	67.1 \pm 0.9	0.96	0.06
MEANMIL [Lerousseau et al., 2021] (20 \times)	63.5 \pm 1.1	65.9 \pm 1.6	0.96	0.06
SPARSECONVMIL [Lerousseau et al., 2021] (20 \times)	67.7 \pm 0.6	68.7 \pm 0.1	0.96	0.06
ABMIL [Isle et al., 2018] (20 \times)	83.2 \pm 1.7	84.0 \pm 1.3	39.12	13.92
CLAM-SB [Lu et al., 2021a] (20 \times)	83.3 \pm 1.5	84.0 \pm 1.3	39.12	13.92
TRANSMIL [Shao et al., 2021] (20 \times)	83.6\pm2.6	85.3\pm1.9	39.12	13.92
ZOONMIL (10 \times \rightarrow 20 \times)	<u>83.3\pm0.3</u>	<u>84.2\pm0.4</u>	14.94	5.32

BRIGHT WSIs are 4.5 \times larger than INSEC WSIs, thus providing better evaluation ground for efficient scaling. ZOONMIL achieves the best performance, outperforming CLAM-SB and TRANSMIL by 5.2% and 2.8% in weighted F1-score. Notably, ZOONMIL-EFF achieves the second best results by a margin of 2.9% and 0.5% over CLAM-SB and TRANSMIL. For the individual classes, ZOONMIL reaches an average F1-score of 70.4%, 56.5%, and 77.8%. The performance is lowest for the pre-cancerous class, which is typically very challenging to identify and often ambiguous with the other two categories.

We also benchmark ZOONMIL on the popular CAMELYON16 dataset. As the metastatic regions can be extremely small (see Figure 4), we set the lowest magnification to 10 \times in ours. Nevertheless, this still has an adverse impact on the performance, resulting in 1.1% lower average accuracy than TRANSMIL. However, it translates to misclassifying only one to two WSIs in the test set.

Overall, our proposed method achieves better classification performance on INSEC and BRIGHT, while being comparable to the state of the art on CAMELYON16. ZOONMIL also consistently outperforms ZOONMIL-EFF, highlighting the apparent performance-efficiency trade-off, *i.e.*, performance reduction in exchange for gains in computational efficiency.

4.3.2 Efficiency measurements

We conduct an efficiency analysis, in terms of FLOPs and processing time for running inference, on INSEC, BRIGHT, and CAMELYON16 (see Table 1, 2, and 3). On INSEC and BRIGHT, ZOONMIL uses \approx 10 \times less FLOPs and processing time than the best performing baselines, CLAM-SB and TransMIL. On BRIGHT, our efficient variant reduces computational requirements and time by more than 40 \times compared to CLAM-SB and TransMIL while providing comparable performance. On CAMELYON16, ZOONMIL uses approximately a third of the number of FLOPs required by CLAM-SB and TransMIL. The relatively lower efficiency gain is due to the task itself, where metastases regions include only a small fraction of the WSI, and thus, need to be analysed at a finer magnification. On all considered datasets, the methods adopting random patch selection (MAXMIL, MEANMIL and SPARSECONVMIL) highlight similar computational requirements as ZOONMIL, but perform significantly worse, with >10% accuracy drop on CAMELYON16 and BRIGHT.

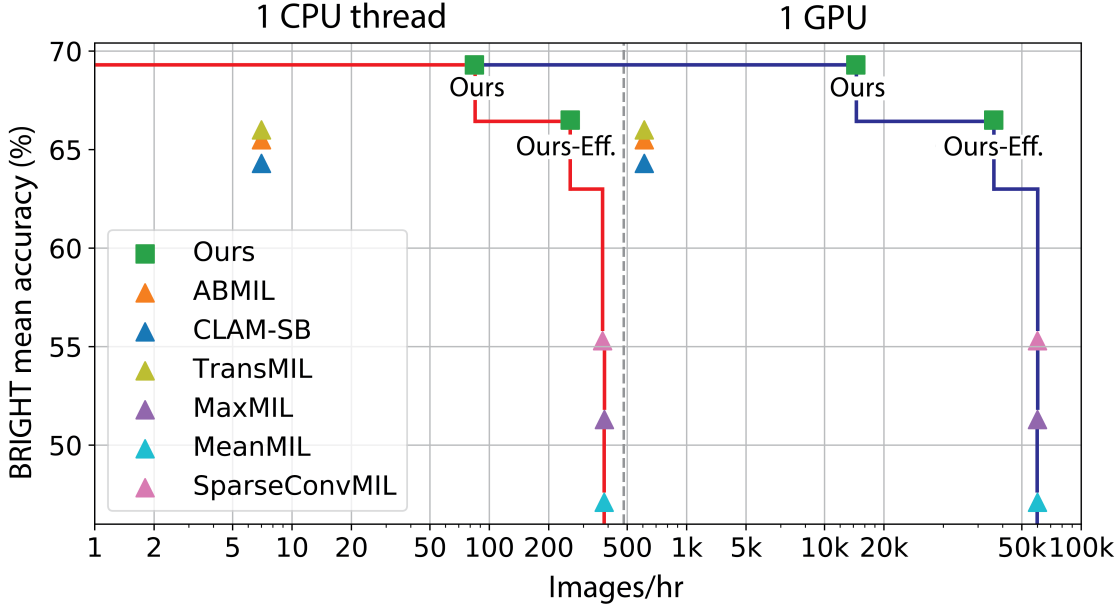


Figure 3: Throughput vs classification accuracy for different MIL methods on BRIGHT, (left) on 1 single-core CPU, (right) on 1 NVIDIA A-100 GPU. Efficiency frontier curves are in red and blue for CPU and GPU, respectively

To further showcase the efficiency gain of ZOONMIL, Figure 3 presents the model throughput (images/hour) against performance (accuracy) for all methods on BRIGHT. The marked efficiency frontier curves signify the best possible accuracies for different minimal throughput requirements. Noticeably, ZOONMIL-EFF running on a single-core CPU processor (300 images/h) provides similar throughput to TransMIL and CLAM-SB running on a cutting-edge NVIDIA A100 GPU (600 images/h). The low computational requirements of ZOONMIL makes it more practical and adapted for deployment in clinics, where IT infrastructures are often poorly developed and need large investments for acquiring and maintaining a digital workflow.

4.3.3 Interpretability

We interpret ZOONMIL by qualitatively analyzing its patch-level attention maps. Figure 4(a,b) demonstrate the maps for two cancerous WSIs in BRIGHT, extracted at $1.25\times$, and Figure 4(c-f) show the maps for four metastatic WSIs in CAMELYON16, extracted at $10\times$. We have further included corresponding tumor regions for each WSI, annotated by an expert pathologist, for comparison. Brighter regions in the attention maps indicate higher attention scores, *i.e.*, more influential regions towards the model’s prediction.

For the BRIGHT WSIs, ZOONMIL correctly attends to cancerous areas in (a,b), pays lower attention to pre-cancerous area in (b), and the least attention to the remaining non-cancerous areas, that include non-cancerous epithelium, stroma, and adipose tissue. For the CAMELYON16 WSIs, (c,d) are correctly classified as ZOONMIL gives high attention to the metastatic regions of different sizes. However, the extremely small metastases in (e,f) get low attention, and get disregarded by the Top-K module leading to misclassifying the WSIs. Notably, for cases with tiny metastases, relatively higher attention is imparted on the periphery of the tissues. This is consistent with the fact that metastases generally appear in the subcapsular zone of lymph nodes, as can be observed in (c-f). The presented visualizations are obtained from low magnifications in ZOONMIL, which signifies the learnability of the method to zoom in. More interpretability maps for other classes, and fine-grained attention maps from higher attention modules in ZOONMIL are provided in the supplemental material.

4.3.4 Ablation study

We ablated different modules in ZOONMIL-EFF, due to its simple 2-magnification model. The results on BRIGHT are given in Table 4.

Differentiable patch selection: We compared our attention-based differentiable patch selection (DIFF-TOPK) against three alternatives: random selection at the lowest magnification (RANDOM K @ $1.25\times$), random selection at the highest magnification (RANDOM 4K @ $2.5\times$), and the non-differentiable Top-K selection (NONDIFF-TOPK) at the

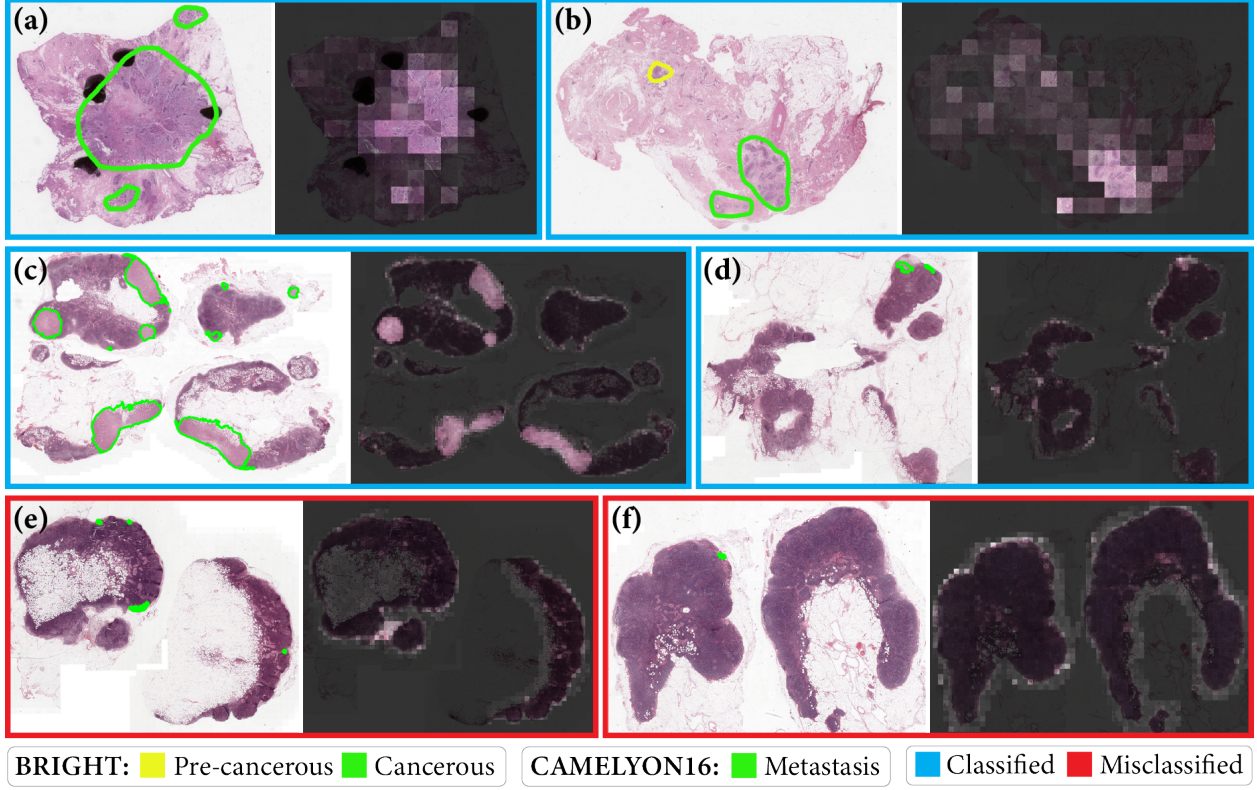


Figure 4: Annotated tumor regions and attention maps from the lowest magnification of ZOONMIL are presented for (a,b) BRIGHT and (c-f) CAMELYON16 WSIs

Table 4: Ablation study on BRIGHT dataset, with the varied algorithmic aspect tabulated in the left-most column. All experiments use $K = 8$

	Methods	Weighted F1(%)	Accuracy(%)
Patch sel.	RANDOM K @ 1.25 \times	61.0	61.0
	RANDOM 4K @ 2.5 \times	59.6	60.0
	NONDIFF-TOPK K @ 1.25 \times	59.9	60.0
	DIFF-TOPK K @ 1.25 \times (Ours)	68.1	68.0
Attn.	Single GA @ 1.25 \times	59.6	61.0
	DGA @ 1.25 \times (Ours)	68.1	68.0
Feat.	Features @2.5 \times	62.7	63.5
	Features @1.25 \times @2.5 \times	64.9	65.0
	Features @1.25 \times + @2.5 \times (Ours)	68.1	68.0

lowest magnification. The top rows in Table 4 show the superiority of DIFF-TOPK. It is due to the differentiability of DIFF-TOPK, that learns to select patches via the gradient-optimization of the model’s prediction.

Dual gated attention: We examined DGA consisting of two separate gated attention modules GA_1 and GA'_1 at low magnification, as discussed in Section 3.3. The former computes a slide-level representation and the latter learns to select patches at higher magnification. We can conclude from Table 4 that two separate attentions lead to better patch selection and improved slide representation for overall improved classification.

Feature aggregation: As shown in Eq. (7), we aggregate slide-level representations across magnifications through sum-pooling. Among several alternatives, we compared with: using the highest magnification features (Features@2.5 \times), and fusing representations via concatenation (herein represented as @1.25 \times || @2.5 \times). Concatenation improved performance, as shown in Table 4, indicating the value of multi-scale information. However, a sum is more natural comparatively, when the two inputs are closely related. Our sum-pooling operation is inspired by residual learning,

which utilizes the complementarity of two inputs [He et al., 2016]. The gain is substantiated in Table 4, where sum-pooling significantly outperforms concatenation.

5 Conclusion

In this work, we introduced ZOOMMIL, a novel framework for WSI classification. The method is more than an order of magnitude faster than previous state-of-the-art methods during inference, while achieving comparable or better accuracy. Essential for our method is the concept of differentiable zooming that allows the model to learn which patches are informative and thus worth zooming-in to. We conduct extensive quantitative and qualitative evaluations on three different datasets, and demonstrate the importance of each component in our model with a detailed ablation study. Finally, we show that ZOOMMIL is a modular architecture, that can easily be deployed in different flavors, depending on the performance-efficiency requirements in a given application.

References

D.S. Gomes, S.S. Porto, D. Balabram, and H. Gobbi. Inter-observer variability between general pathologists and a specialist in breast pathology in the diagnosis of lobular neoplasia, columnar cell lesions, atypical ductal hyperplasia and ductal carcinoma in situ of the breast. *Diagnostic Pathology*, 9:1–9, 2014.

J.G. Elmore, G.M. Longton, P.A. Carney, B.M. Geller, T. Onega, A.N.A. Tosteson, H.D. Nelson, M.S. Pepe, K.H. Allison, S.J. Schnitt, et al. Diagnostic concordance among pathologists interpreting breast biopsy specimens. *JAMA*, 313:1122–1132, 2015.

G. Campanella, M.G. Hanna, L. Geneslaw, A. Miraflor, V. Werneck Krauss Silva, K.J. Busam, E. Brogi, V.E. Reuter, D.S. Klimstra, and T.J. Fuchs. Clinical-grade computational pathology using weakly supervised deep learning on whole slide images. *Nature Medicine*, 25:1301–1309, 2019.

M.Y. Lu, D.F.K. Williamson, T.Y. Chen, R.J. Chen, M. Barbieri, and F. Mahmood. Data efficient and weakly supervised computational pathology on whole slide images. *Nature Biomedical Engineering*, 5:555–570, 2021a.

D. Tellez, G. Litjens, J. van der Laak, and F. Ciompi. Neural image compression for gigapixel histopathology image analysis. *IEEE Transactions on Pattern Analysis and Machine Intelligence*, 43:567–578, 2019.

M. Shaban, R. Awan, M.M. Fraz, A. Azam, Y. Tsang, D. Snead, and N.M. Rajpoot. Context-aware convolutional neural network for grading of colorectal cancer histology images. *IEEE Transactions on Medical Imaging*, 39:2395–2405, 2020.

Z. Jia, X. Huang, I. Eric, C. Chang, and Y. Xu. Constrained deep weak supervision for histopathology image segmentation. *IEEE Transactions on Medical Imaging*, 36:2376–2388, 2017.

Q. Liang, Y. Nan, G. Coppola, K. Zou, W. Sun, D. Zhang, Y. Wang, and G. Yu. Weakly supervised biomedical image segmentation by reiterative learning. *IEEE Journal of Biomedical and Health Informatics*, 23:1205–1214, 2018.

J. Yao, X. Zhu, J. Jonnagaddala, N. Hawkins, and J. Huang. Whole slide images based cancer survival prediction using attention guided deep multiple instance learning networks. *Medical Image Analysis*, 65, 2020.

P. Pati, G. Jaume, A. Foncubierta-Rodríguez, F. Feroce, A.M. Anniciello, G. Scognamiglio, N. Brancati, M. Fiche, E. Dubruc, D. Riccio, et al. Hierarchical graph representations in digital pathology. *Medical Image Analysis*, 75, 2021.

B.E. Bejnordi, G. Zuidhof, M. Balkenhol, M. Hermsen, P. Bult, B. van Ginneken, N. Karssemeijer, G. Litjens, and J. van der Laak. Context-aware stacked convolutional neural networks for classification of breast carcinomas in whole-slide histopathology images. *Journal of Medical Imaging*, 4, 2017a.

K. Sirinukunwattana, N.K. Alham, C. Verrill, and J. Rittscher. Improving whole slide segmentation through visual context - a systematic study. In *International Conference on Medical Image Computing and Computer Assisted Intervention (MICCAI)*, pages 192–200, 2018.

A. Myronenko, Z. Xu, D. Yang, H.R. Roth, and D. Xu. Accounting for dependencies in deep learning based multiple instance learning for whole slide imaging. In *International Conference on Medical Image Computing and Computer Assisted Intervention (MICCAI)*, pages 329–338, 2021.

Z. Shao, H. Bian, Y. Chen, Y. Wang, J. Zhang, X. Ji, and Y. Zhang. Transmil: Transformer based correlated multiple instance learning for whole slide image classification. In *Advances in Neural Information Processing Systems (NeurIPS)*, volume 35, 2021.

M. Lerousseau, M. Vakalopoulou, E. Deutsch, and N. Paragios. Sparseconvmil: Sparse convolutional context-aware multiple instance learning for whole slide image classification. In *MICCAI Workshop on Computational Pathology*, pages 129–139, 2021.

N. Hashimoto, D. Fukushima, R. Koga, Y. Takagi, K. Ko, K. Kohno, M. Nakaguro, S. Nakamura, H. Hontani, and I. Takeuchi. Multi-scale domain-adversarial multiple-instance cnn for cancer subtype classification with unannotated histopathological images. In *IEEE Conference on Computer Vision and Pattern Recognition (CVPR)*, pages 3852–3861, 2020.

D.J. Ho, D.V.K. Yarlagadda, T.M. D’Alfonso, M.G. Hanna, A. Grabenstetter, P. Ntiamoah, E. Brogi, L.K. Tan, and T.J. Fuchs. Deep multi-magnification networks for multi-class breast cancer image segmentation. *Computerized Medical Imaging and Graphics*, 88, 2021.

J. Deng, W. Dong, R. Socher, L. Li, K. Li, and L. Fei-Fei. Imagenet: A large-scale hierarchical image database. In *IEEE Conference on Computer Vision and Pattern Recognition (CVPR)*, pages 248–255, 2009.

K. He, X. Zhang, S. Ren, and J. Sun. Deep residual learning for image recognition. In *IEEE Conference on Computer Vision and Pattern Recognition (CVPR)*, pages 770–778, 2016.

M. Isle, J. Tomczak, and M. Welling. Attention-based deep multiple instance learning. In *International Conference on Machine Learning (ICML)*, volume 35, 2018.

M.Y. Lu, T.Y. Chen, D.F.K. Williamson, M. Zhao, M. Shady, J. Lipkova, and F. Mahmood. Ai-based pathology predicts origins for cancers of unknown primary. *Nature*, 594:106–110, 2021b.

B.E. Bejnordi, G. Litjens, M. Hermsen, N. Karssemeijer, and J. van der Laak. A multi-scale superpixel classification approach to the detection of regions of interest in whole slide histopathology images. In *SPIE Medical Imaging 2015: Digital Pathology*, volume 9420, 2015.

Y. Gao, W. Liu, S. Arjun, L. Zhu, V. Ratner, T. Kurc, J. Saltz, and A. Tannenbaum. Multi-scale learning based segmentation of glands in digital colorectal pathology images. In *SPIE Medical Imaging 2016: Digital Pathology*, volume 9791, 2016.

H. Tokunaga, Y. Teramoto, A. Yoshizawa, and R. Bise. Adaptive weighting multi-field-of-view cnn for semantic segmentation in pathology. In *IEEE Conference on Computer Vision and Pattern Recognition (CVPR)*, pages 12597–12606, 2019.

J. Li, W. Li, A. Sisk, H. Ye, W. D. Wallace, W. Speier, and C.W. Arnold. A multi-resolution model for histopathology image classification and localization with multiple instance learning. *Computers in Biology and Medicine*, 131, 2021a.

B. Li, Y. Li, and K.W. Eliceiri. Dual-stream multiple instance learning network for whole slide image classification with self-supervised contrastive learning. In *IEEE Conference on Computer Vision and Pattern Recognition (CVPR)*, pages 14318–14328, 2021b.

B. Aygüneş, S. Aksoy, R.G. Cinbiş, K. Kösemehmetoğlu, S. Önder, and A. Üner. Graph convolutional networks for region of interest classification in breast histopathology. In *SPIE Medical Imaging 2020: Digital Pathology*, volume 11320, 2020.

Y. Zhao, F. Yang, Y. Fang, H. Liu, N. Zhou, J. Zhang, J. Sun, S. Yang, B. Menze, X. Fan, et al. Predicting lymph node metastasis using histopathological images based on multiple instance learning with deep graph convolution. In *IEEE Conference on Computer Vision and Pattern Recognition (CVPR)*, pages 4837–4846, 2020.

A. Raju, J. Yao, M.M. Haq, J. Jonnagaddala, and J. Huang. Graph attention multi-instance learning for accurate colorectal cancer staging. In *International Conference on Medical Image Computing and Computer Assisted Intervention (MICCAI)*, pages 529–539, 2020.

R. Li, J. Yao, X. Zhu, Y. Li, and J. Huang. Graph cnn for survival analysis on whole slide pathological images. In *International Conference on Medical Image Computing and Computer-Assisted Intervention (MICCAI)*, pages 174–182, 2018.

M. Adnan, S. Kalra, and H.R. Tizhoosh. Representation learning of histopathology images using graph neural networks. In *IEEE Conference on Computer Vision and Pattern Recognition (CVPR) Workshops*, pages 988–989, 2020.

V. Anklin, P. Pati, G. Jaume, B. Bozorgtabar, A. Foncubierta-Rodriguez, J.P. Thiran, M. Sibony, M. Gabrani, and O. Goksel. Learning whole-slide segmentation from inexact and incomplete labels using tissue graphs. In *International Conference on Medical Image Computing and Computer Assisted Intervention (MICCAI)*, pages 636–646, 2021.

N. Dong, M. Kampffmeyer, X. Liang, Z. Wang, W. Dai, and E. Xing. Reinforced auto-zoom net: Towards accurate and fast breast cancer segmentation in whole-slide images. In *International Conference on Medical Image Computing and Computer Assisted Intervention (MICCAI) Workshop*, pages 317–325, 2018.

T. Qaiser and N.M. Rajpoot. Learning where to see: A novel attention model for automated immunohistochemical scoring. *IEEE Transactions on Medical Imaging*, 38:2620–2631, 2019.

A. BenTaieb and G. Hamarneh. Predicting cancer with a recurrent visual attention model for histopathology images. In *International Conference on Medical Image Computing and Computer Assisted Intervention (MICCAI)*, pages 129–137, 2018.

S. Kong and R. Henao. Efficient classification of very large images with tiny objects. *arXiv:2106.02694*, 2021.

A. Katharopoulos and F. Fleuret. Processing megapixel images with deep attention-sampling models. In *International Conference on Machine Learning (ICML)*, volume 36, 2019.

Q. Berthet, M. Blondel, O. Teboul, M. Cuturi, J.P. Vert, and F. Bach. Learning with differentiable perturbed optimizers. In *Advances in Neural Information Processing Systems (NeurIPS)*, volume 34, pages 9508–9519, 2020.

J.B. Cordonnier, A. Mahendran, and A. Dosovitskiy. Differentiable patch selection for image recognition. In *IEEE Conference on Computer Vision and Pattern Recognition (CVPR)*, pages 2351–2360, 2021.

S.P. Oliveira, P.C. Neto, J. Fraga, D. Montezuma, A. Monteiro, J. Monteiro, L. Ribeiro, S. Gonçalves, I.M. Pinto, and J.S. Cardoso. Cad systems for colorectal cancer from wsi are still not ready for clinical acceptance. *Scientific Reports*, 11, 2021.

N. Brancati, A.M. Anniciello, P. Pati, D. Riccio, G. Scognamiglio, G. Jaume, G. De Pietro, M. Di Bonito, A. Foncubierta-Rodríguez, G. Botti, et al. Bracs: A dataset for breast carcinoma subtyping in h&e histology images. *arXiv:2111.04740*, 2021.

B.E. Bejnordi, M. Veta, P.J. van Dienst, B. van Ginneken, N. Karssemeijer, G. Litjens, J. van der Laak, et al. Diagnostic assessment of deep learning algorithms for detection of lymph node metastases in women with breast cancer. *JAMA*, 318:2199–2210, 2017b.

G. Jaume, P. Pati, V. Anklin, A. Foncubierta-Rodríguez, and M. Gabrani. Histocartography: A toolkit for graph analytics in digital pathology. In *MICCAI Workshop on Computational Pathology*, 2021.

A. Paszke, S. Gross, F. Massa, A. Lerer, J. Bradbury, G. Chanan, T. Killeen, Z. Lin, N. Gimelshein, L. Antiga, et al. Pytorch: An imperative style, high-performance deep learning library. In *Advances in Neural Information Processing Systems (NeurIPS)*, volume 33, pages 8024–8035, 2019.

D.P. Kingma and J.L. Ba. Adam: A method for stochastic optimization. In *International Conference on Learning Representations (ICLR)*, 2015.

M.R. Zhang, J. Lucas, G. Hinton, and J. Ba. Lookahead optimizer: k steps forward, 1 step back. In *Advances in Neural Information Processing Systems (NeurIPS)*, volume 33, 2019.

Supplemental Material

In this supplemental material, we include additional results, visualizations, and analyses. The contents of the individual sections are:

- Appendix A: Confusion matrices for ZOONMIL on all datasets. Additional results for the competing methods operating at different magnifications
- Appendix B: Analyzing the limitations of ZOONMIL
- Appendix C: Analyzing the impact of the number of selected patches in the differentiable Top-K module
- Appendix D: ZOONMIL attention maps at different magnifications
- Appendix E: Training details of the competing baselines
- Appendix F: Derivation of the Jacobian for differentiable patch selection

A Additional Classification Analysis

In Figure 5, we present the confusion matrices of ZOONMIL on all datasets. Results are averaged over three runs with different weight initializations. On INSEC, ZOONMIL performs very well and correctly classifies 95.63% and 94.55% of the non-neoplastic and low-grade cases, respectively. Out of all high-grade, cases, our model identifies 83.33% correctly. We can see that BRIGHT is the most difficult dataset due to its challenging pre-cancerous class, which is often confused with either the non-cancerous or the cancerous class. On CAMELYON16, ZOONMIL accurately identifies 97.92 % of non-metastatic cases, while correctly classifying 61.90 % of metastatic cases.

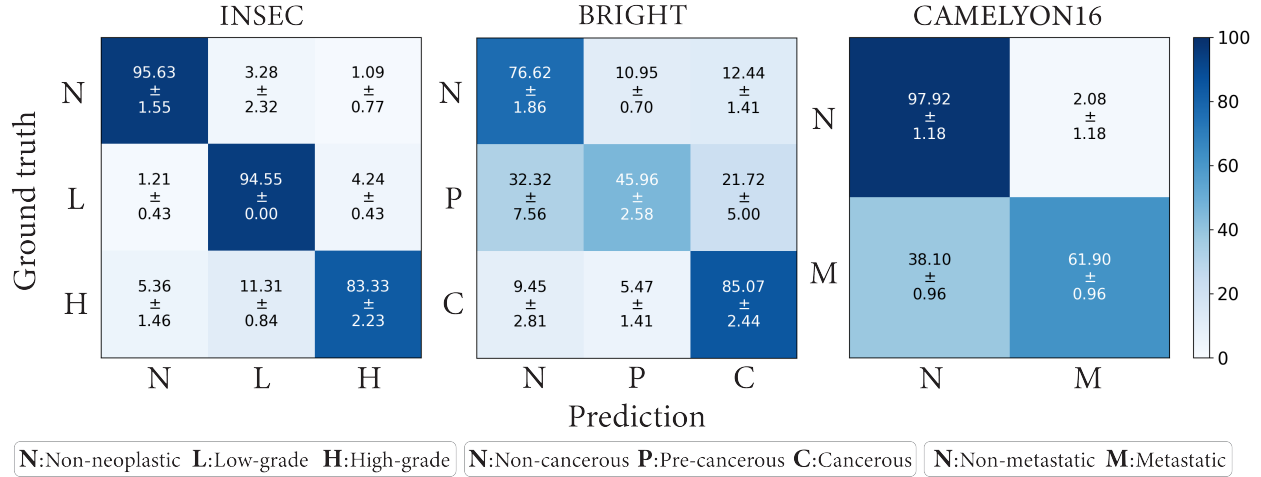


Figure 5: Confusion matrices of ZOONMIL on INSEC, BRIGHT, and CAMELYON16. An entry represents the corresponding fraction (%) w.r.t. all samples in the same row

Additionally, we report the classification performance of all baselines operating at different magnifications in Table 5, 6, and 7. It can be observed in Table 5 and 6 that lower magnifications severely impact the performance of the baselines, while ZOONMIL-EFF performs significantly better. These results indicate the efficacy of our method, and conclude the benefits of zooming and combining information across magnifications.

B Limitations

We conjecture that our classification performance on CAMELYON16 is limited by the size of the metastatic regions. For the samples including extremely small metastases, it is challenging to optimize the zooming process. To validate our hypothesis, we sub-categorize the metastatic samples in the training set into “small” and “large” metastatic groups, via visual inspection, and create new stratified training and validation sets. In Table 8, we present the classification performances of ZOONMIL on the validation set, individually for the small and large metastatic samples. The results show that the performance is significantly higher for large metastases, which substantiates our hypothesis.

Table 5: Classification performances on the INSEC dataset [Oliveira et al., 2021]

Methods	Classification	
	Weighted-F1(%)	Accuracy(%)
ABMIL [Isle et al., 2018] (5 \times)	86.8 \pm 0.7	87.0 \pm 0.7
ABMIL [Isle et al., 2018] (10 \times)	88.8 \pm 0.7	89.0 \pm 0.6
CLAM-SB [Lu et al., 2021a] (5 \times)	87.7 \pm 0.5	87.8 \pm 0.5
CLAM-SB [Lu et al., 2021a] (10 \times)	89.5 \pm 0.5	89.6 \pm 0.5
TRANSMIL [Shao et al., 2021] (5 \times)	86.2 \pm 1.1	87.4 \pm 1.1
TRANSMIL [Shao et al., 2021] (10 \times)	88.4 \pm 1.3	89.1 \pm 1.1
ZOOMBIL-EFF (5 \times \rightarrow 10 \times)	90.3 \pm 1.3	90.3 \pm 1.3
ZOOMBIL (5 \times \rightarrow 10 \times \rightarrow 20 \times)	92.0 \pm 0.6	92.1 \pm 0.7

Table 6: Classification performances on the BRIGHT dataset [Brancati et al., 2021]

Methods	Classification	
	Weighted-F1(%)	Accuracy(%)
ABMIL [Isle et al., 2018] (1.25 \times)	58.4 \pm 1.0	58.9 \pm 1.6
ABMIL [Isle et al., 2018] (2.5 \times)	58.7 \pm 1.1	59.3 \pm 1.0
CLAM-SB [Lu et al., 2021a] (1.25 \times)	59.9 \pm 1.3	60.3 \pm 1.2
CLAM-SB [Lu et al., 2021a] (2.5 \times)	60.1 \pm 1.2	60.2 \pm 1.6
TRANSMIL [Shao et al., 2021] (1.25 \times)	46.1 \pm 3.8	47.3 \pm 2.5
TRANSMIL [Shao et al., 2021] (2.5 \times)	52.0 \pm 1.3	54.5 \pm 2.7
ZOOMBIL-EFF (1.25 \times \rightarrow 2.5 \times)	66.0 \pm 1.9	66.5 \pm 1.5
ZOOMBIL (1.25 \times \rightarrow 2.5 \times \rightarrow 10 \times)	68.3 \pm 1.1	69.3 \pm 1.0

Table 7: Classification performances on the CAMELYON16 dataset [Bejnordi et al., 2017b]

Methods	Classification	
	Weighted-F1(%)	Accuracy(%)
ABMIL [Isle et al., 2018] (10 \times)	76.7 \pm 0.8	78.3 \pm 0.7
CLAM-SB [Lu et al., 2021a] (10 \times)	77.5 \pm 0.6	79.1 \pm 0.6
TRANSMIL [Shao et al., 2021] (10 \times)	76.6 \pm 1.1	79.6 \pm 1.0
ZOOMBIL (10 \times \rightarrow 20 \times)	83.3 \pm 0.3	84.2 \pm 0.4

Table 8: Classification performances on the validation set of CAMELYON16 [Bejnordi et al., 2017b]. Validation set is further grouped according to the size of the metastatic regions

Size of metastases	Classification	
	Weighted-F1(%)	Accuracy(%)
large	96.2 \pm 1.0	96.1 \pm 1.1
small	86.7 \pm 1.0	87.1 \pm 1.0

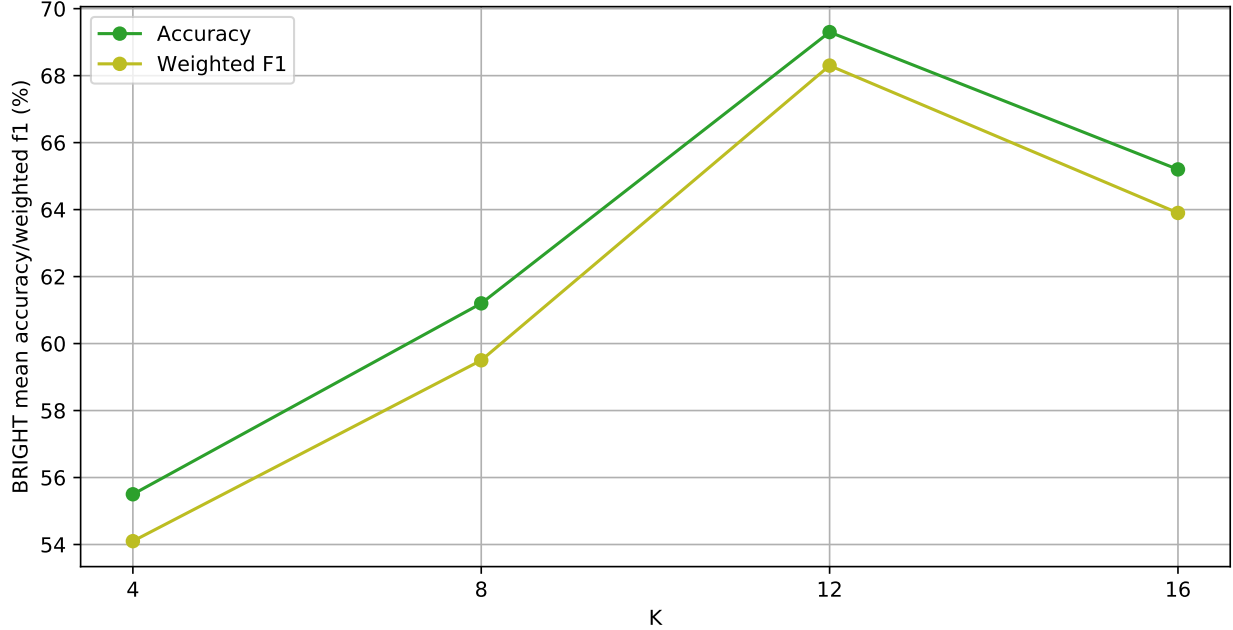


Figure 6: Classification performance of ZOOMBIL on BRIGHT for different values of K

C Impact of K in Differentiable Top-K Patch Selection

Here, we analyze the impact of the number of selected patches (K) on the classification performance of ZOOMBIL. Figure 6 shows that the performance increases with increasing K . It peaks at $K = 12$ and then slightly drops for further increment. We reason that this behavior is caused by the average number of patches per WSI being 16 in the BRIGHT dataset at the lowest magnification ($1.25\times$). Almost all patches are selected in this case, which makes it suboptimal to learn to improve the zooming process.

D Interpretability

We have shown the ZOOMBIL attention maps at the lowest magnification, *i.e.*, $1.25\times$, on the BRIGHT dataset in Figure 4 of the main manuscript. Here, in Figure 7, we provide the attention maps at both low and high magnification, *i.e.*, $1.25\times$ and $10\times$, as well as close-up patches with highest attention scores. We can observe in the zooming process from $1.25\times$ to $10\times$, that the model pins down its focus to the most informative regions in the WSI. The observation is further substantiated by the high attention patches that include cancerous content, *i.e.*, invasive tumors and ductal carcinoma in situ tumors, for the presented cancerous WSIs. Figure 8 shows more examples of annotated tumor regions and attention maps for correctly classified and misclassified samples across all the classes in BRIGHT. For both the correct and incorrect classifications, we can notice that the focus of the model is aligning with the focus of the pathologist. However, the morphological ambiguities among the classes finally lead to certain misclassifications.

E Implementation Details

ABMIL: We follow the network architecture proposed in [Isle et al., 2018]. The model comprises of a gated attention module consisting of three 2-layer MLPs, where the first two are followed by Hyperbolic Tangent and Sigmoid activations, and a 2-layer MLP classifier with ReLU activation.

CLAM-SB: We implement CLAM-SB [Lu et al., 2021a] with the code³ provided by the authors. We use the Adam optimizer [Kingma and Ba, 2015] with 0.0001 learning rate. The maximum and minimum epochs are set to 100, 50, respectively, and use early stopping with patience=20 epochs based on the validation weighted F1 score (for BRIGHT) and validation loss (for INSEC and CAMELYON16). We use cross-entropy loss for both bag loss and instance loss. The weights of bag-level losses are set to 0.7, 0.5, 0.7, and the number of positive/negative patches sampled for instance

³<https://github.com/mahmoodlab/CLAM>

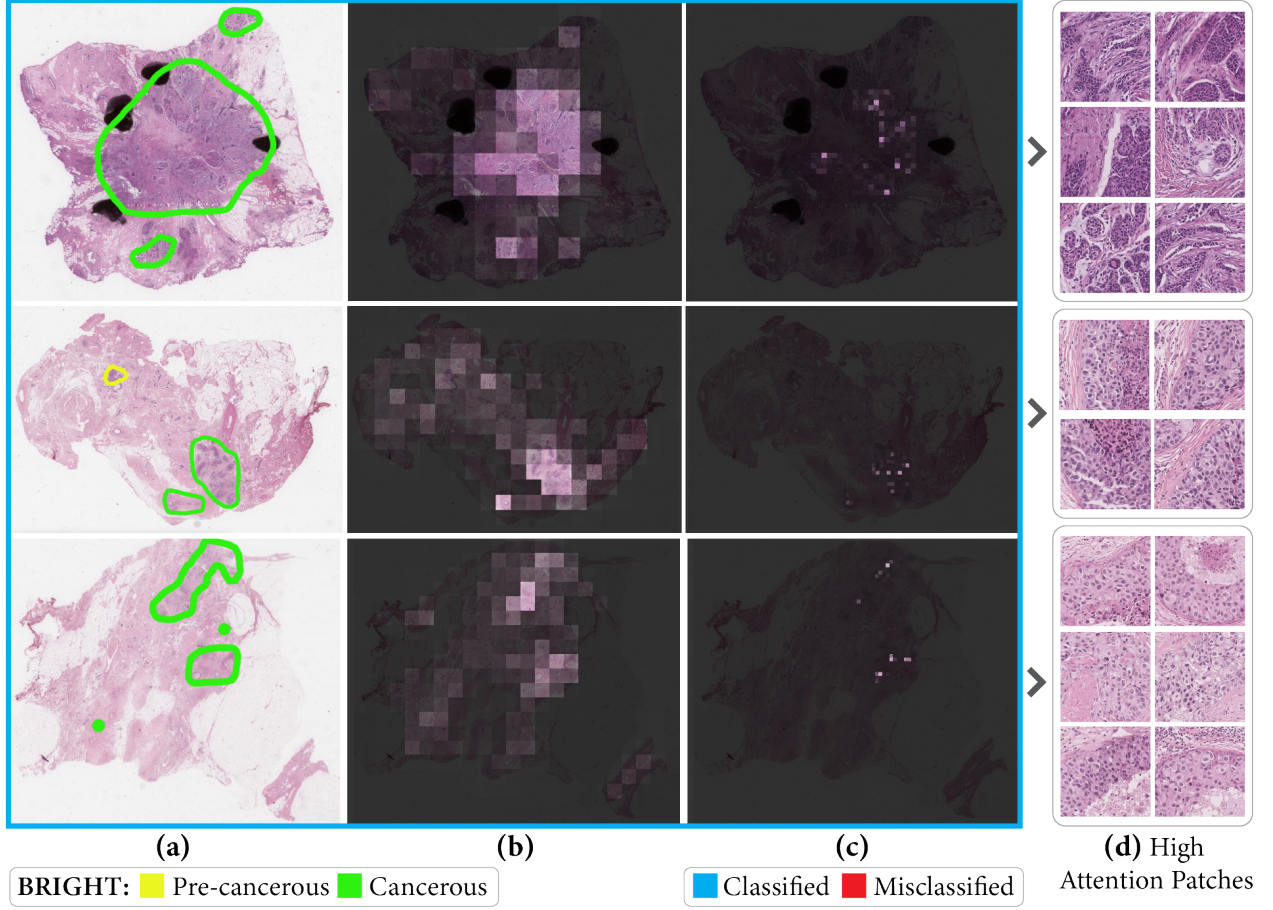


Figure 7: Interpreting ZOONMIL on the BRIGHT dataset: (a) annotated tumor regions, (b) attention maps at $1.25\times$ magnification, (c) attention maps at $10\times$ magnification, and (d) a subset of extracted patches with high attention scores at $10\times$ magnification

loss are set to 8, 32, 32 for INSEC, BRIGHT and CAMELYON16, respectively. For all three datasets we use a weighted sampler due to class imbalance.

TransMIL: We adopt the original implementation⁴ of TransMIL [Shao et al., 2021]. We use Lookahead optimizer [Zhang et al., 2019] with learning rate 0.0002 and weight decay 0.00001. The maximum epochs are set to 200 and early stopping is used with a *patience* of 10 epochs based on validation weighted F1 score (for BRIGHT) and validation loss (for INSEC and Camelyon). We use cross-entropy loss as training loss.

SparseConvMIL: We adopt the original implementation⁵ of SparseConvMIL [Lerousseau et al., 2021]. Unlike other baselines, we run the model on a V100 GPU with 32GB RAM, as it depends on SparseConvNet⁶. Therefore, we limit the batch size and the number of sampled patches to 8 and 100, respectively. In the model, we set the number of sparseconv channels to 32, the downsampling factor of the sparse map to 128, and the neurons in the MLP classifier to 128. We use ResNet34 for extracting patch features, and finetune it with learning rate 0.00001. The learning rate for the rest of the model is 0.001, and weight decay is 0.0001.

Max & Mean MIL: We use the formulation presented in [Lerousseau et al., 2021] for Max and Mean MIL. We set the same values for the hyperparameters as in SparseConvMIL, but freeze the patch feature extractor, *i.e.*, ResNet34.

⁴<https://github.com/szc19990412/TransMIL>

⁵<https://github.com/MarvinLer/SparseConvMIL>

⁶<https://github.com/facebookresearch/SparseConvNet>

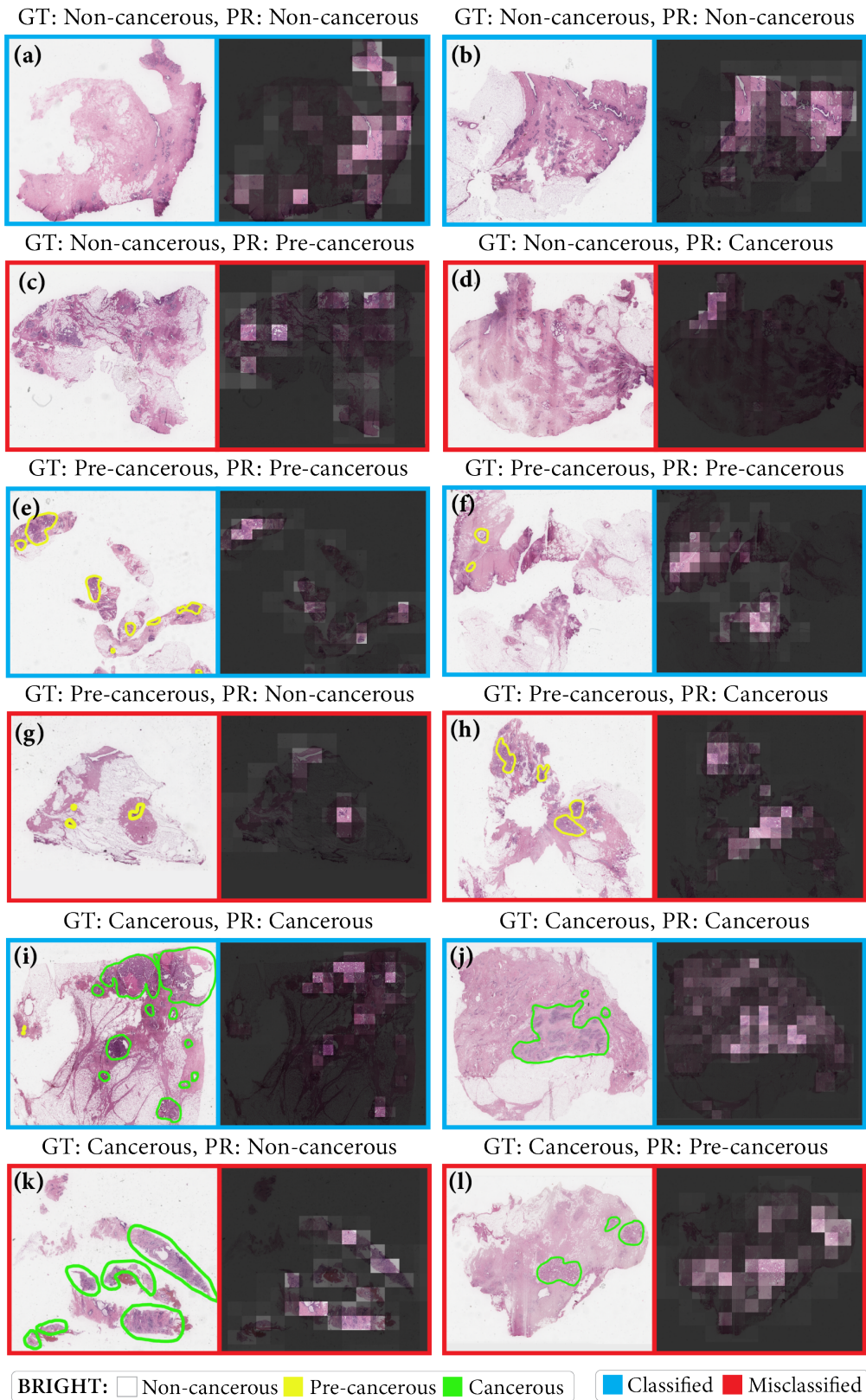


Figure 8: Examples of BRIGHT WSIs with annotated tumor regions and attention maps from ZOOMMIL at $1.25\times$ magnification

F Derivation of Jacobian for Differentiable Patch Selection

F.1 Perturbed Maximum

As described in [Berthet et al., 2020], given a set of distinct points $\mathcal{T} \subset \mathbb{R}^d$ and its convex hull \mathcal{C} , a discrete optimization problem with inputs $\mathbf{a}_m \in \mathbb{R}^d$ can generally be formulated as:

$$\max_{\hat{\mathbf{t}} \in \mathcal{C}} \langle \hat{\mathbf{t}}, \mathbf{a}_m \rangle \quad \mathbf{t} = \arg \max_{\hat{\mathbf{t}} \in \mathcal{C}} \langle \hat{\mathbf{t}}, \mathbf{a}_m \rangle. \quad (8)$$

As per Definition 2.1 in [Berthet et al., 2020], we can obtain a smoothed \mathbf{t} by adding a random noise vector $\sigma \mathbf{Z} \in \mathbb{R}^d$ with distribution $d\mu(\mathbf{z}) \propto \exp(-\nu(\mathbf{z}))d\mathbf{z}$, where $\sigma > 0$ is a scaling parameter. The perturbed version of the maximizer in Eq. (8) then becomes:

$$\mathbf{t} = \mathbb{E} \left[\arg \max_{\hat{\mathbf{t}} \in \mathcal{C}} \langle \hat{\mathbf{t}}, \mathbf{a}_m + \sigma \mathbf{Z} \rangle \right]. \quad (9)$$

According to Proposition 3.1 from [Berthet et al., 2020], the associated Jacobian matrix of \mathbf{t} at \mathbf{a}_m can then be computed as follows:

$$J_{\mathbf{a}_m} \mathbf{t} = \mathbb{E} \left[\arg \max_{\hat{\mathbf{t}} \in \mathcal{C}} \langle \hat{\mathbf{t}}, \mathbf{a}_m + \sigma \mathbf{Z} \rangle \nabla_{\mathbf{z}} \nu(\mathbf{Z})^{\top} / \sigma \right]. \quad (10)$$

We choose our noise to have a normal distribution, *i.e.*, $\mathbf{Z} \sim \mathcal{N}(0, \mathbb{1})$. We can thus plug $\nabla_{\mathbf{z}} \nu(\mathbf{Z})^{\top} = \mathbf{Z}^{\top}$ into Eq. (10) and obtain:

$$J_{\mathbf{a}_m} \mathbf{t} = \mathbb{E}_{\mathbf{Z} \sim \mathcal{N}(0, \mathbb{1})} \left[\arg \max_{\hat{\mathbf{t}} \in \mathcal{C}} \langle \hat{\mathbf{t}}, \mathbf{a}_m + \sigma \mathbf{Z} \rangle \mathbf{Z}^{\top} / \sigma \right]. \quad (11)$$

F.2 Differentiable Top-K Operator

As shown in [Cordonnier et al., 2021], the Top-K selection with sorted indices can be converted into the same form as Eq. (8). To this end, the constraint set \mathcal{C} for the indicator matrix $\hat{\mathbf{T}}$ should first be defined as:

$$\mathcal{C} = \left\{ \hat{\mathbf{T}} \in \mathbb{R}^{N \times K} : \quad \hat{\mathbf{T}}_{n,k} \geq 0 \right. \quad (12)$$

$$\left. \sum_{j=1}^N \hat{\mathbf{T}}_{j,k} = 1 \quad \forall k \in \{1, \dots, K\} \right. \quad (13)$$

$$\left. \sum_{k=1}^K \hat{\mathbf{T}}_{j,k} \leq 1 \quad \forall j \in \{1, \dots, N\} \right. \quad (14)$$

$$\left. \sum_{i=1}^N i \hat{\mathbf{T}}_{i,k} < \sum_{j=1}^N j \hat{\mathbf{T}}_{j,k} \quad k < k' \right\}, \quad (15)$$

where Eq. (13) ensures that each column-wise sum in the indicator matrix is equal to one and Eq. (14) constrains each row-wise sum to be at most one. Lastly, Eq. (15) enforces that the indices of the attention weights selected by $\hat{\mathbf{T}}$ are sorted. With these constraints, the general linear program formulation in Eq. (8) can be used to describe the Top-K selection problem:

$$\max_{\hat{\mathbf{T}} \in \mathcal{C}} \langle \hat{\mathbf{T}}, \mathbf{a}_m \mathbf{1}^{\top} \rangle \quad \mathbf{T} = \arg \max_{\hat{\mathbf{T}} \in \mathcal{C}} \langle \hat{\mathbf{T}}, \mathbf{a}_m \mathbf{1}^{\top} \rangle, \quad (16)$$

where $\mathbf{1}^{\top} = [1 \dots 1] \in \mathbb{R}^{1 \times K}$ and thus $\mathbf{a}_m \mathbf{1}^{\top} \in \mathbb{R}^{N \times K}$ is a matrix containing the attention vectors \mathbf{a}_m repeated K times as its columns. Note that here, $\langle \cdot \rangle$ computes the scalar product after vectorizing the matrices.

Now, the perturbed maximizer \mathbf{T} and the corresponding Jacobian $J_{\mathbf{a}_m} \mathbf{T}$ can be computed analogously to Eq. (9) and Eq. (11), as presented in the main paper. In contrast to [Berthet et al., 2020], however, for the Top-K selection problem, it is required to apply the same noise vector $\sigma \mathbf{Z}$ to each column in $\mathbf{a}_m \mathbf{1}^{\top}$. Following the insights from [Cordonnier et al., 2021], we therefore apply in practice the noise directly to \mathbf{a}_m , *i.e.*, we employ $(\mathbf{a}_m + \sigma \mathbf{Z}) \mathbf{1}^{\top}$ instead of $\mathbf{a}_m \mathbf{1}^{\top} + \sigma \mathbf{Z}$.